JOURNAL OF COMPUTATIONAL PHYSICS 114, 9–17 (1994)

Numerical Navier–Stokes Solutions from Gas Kinetic Theory

KUN XU* AND KEVIN H. PRENDERGAST

Department of Astronomy, Columbia University, 538W 120th Street, New York, New York, 10027

Received January 14, 1993; revised December 3, 1993

In order to test the gas-kinetic based hydrodynamic scheme given in paper I (K. H. Prendergast and K. Xu, *J. Comput. Phys.* **109**, 53, 1993) as a Navier–Stokes solver, we extend the scheme to two dimensions and exhibit some Navier–Stokes solutions. The scheme is a high-resolution gas kinetic scheme in both space and time. The advective and diffusive fluxes are coupled and solved at the same time by following the time-dependent velocity distribution function for particles. Numerical results for some well-defined Euler and Navier–Stokes test cases are presented. The Kolmogorov and the laminar boundary layer problems exhibit the dominance of the real viscosity effects. The strong shock interaction test cases show the applicability of the scheme to supersonic gas flow.

I. INTRODUCTION

Solving the full system of Navier–Stokes equations is the ultimate goal of a numerical flow simulation. The past 20 years have seen a considerable development of numerical techniques for solving the lower-order system of hyperbolic conservation laws. One group of high resolution methods solve the Euler equations by adopting second-order extensions of Godunov's first-order scheme and incorporating nonlinear wave propagation, such as the schemes given in Roe [25], Colella [11], van Leer [30], and Harten [14]. The other group uses traditional central difference methods, as did by MacCormack [19] and Jameson *et al.* [16]. The numerical solution of the Navier–Stokes equations in both cases is achieved mainly by treating the advection and diffusion terms sequentially, using central differences for the diffusion terms (Shu *et al.* [29], Koren [17], Martinelli and Jameson [20]).

Another type of gas-dynamical simulation stems from consideration of the underlying physics at the molecular level. The N-body microscopic molecular dynamics and the Monte Carlo method (Bird [4]) track a large number of particles individually to determine thermodynamic and transport properties. Because the number of particles that can be employed in the microscopic simulations of hydrodynamic flows is limited, this imposes some constraints on the accuracy of the description of the flow (Boon [5]). In the theory of gases, the microscopic nature of real systems is usually considered in the framework of the Boltzmann equation. A great deal of literature has been devoted to the question of the relation between the microscopic and macroscopic descriptions of fluids. Owing to the difficulty of the problem, several approximations have been used, such as limiting the phase space by taking a discrete set of possible velocities, as in the Broadwell model [6]. In the last several years, lattice gas Boltzmann equation (LGB) methods have been developed which provide an alternative to molecular dynamics for microscopic simulation of macroscopic fluid dynamical phenomena; in these methods the continuous trajectories of particles in the real phase space are approximated by allowing particles to move along the links of a regular lattice with discrete time steps; "collisions" occur at the nodes of the lattice in such a way as to conserve mass, momentum and energy (Frisch *et al.* [13], Doolen [12], and Qian [24]). Direct simulations of hydrodynamics by solving the approximate Boltzmann equation for time-dependent particle distribution functions were first introduced in the 1960s by Chu [9] and Prendergast [27]. Pullin [23], Perthame [21], and many others have also worked on the Boltzmann equation to develop so-called "Boltzmann-type schemes" (Harten, Lax, and van Leer [15]). In all these "Boltzmann-type schemes," due to an over-simplified numerical approximation, the final numerical dissipation usually depends on the grid size and is large enough to mask the real physical viscosity and conductivity effects.

In order to get the Euler and Navier–Stokes solutions accurately from the gas-kinetic theory, in the first paper by Prendergast and Xu [22] (referred to as paper I hereafter), we developed a new numerical approach to the Bhatnagar–Gross–Krook model [3] (BGK hereafter) of the Boltzmann equation. This scheme differs from any other "Boltzmann-type schemes," in that the integral solution of the BGK model and the collisional conservation constraints are used at the same time. In this paper we extend the one-

* Current Address: Dept. of Mechanical and Aerospace Engineering, P.O. Box CN 5263, D-215A, Princeton University, Princeton, NJ 08544-5263.

0021-9991/94 $6.00

dimensional scheme of paper I to two dimensions and give an analysis of the numerical Navier–Stokes solutions.

This paper is arranged as follows. In Section II we give a detailed description of this finite volume scheme in two dimensions, which uses both the x and y variations of the quantities in the evaluation of numerical fluxes across each cell wall. This property distinguishes it from directional splitting schemes. In Section III, we apply this scheme to some well-studied test cases. The last section is the conclusion.

II. A HYDROCODE IN TWO DIMENSIONS

In paper I, we gave some kinetic theory preliminaries and the numerical scheme in one dimension; here we start from the BGK model in two dimensions (no body force). For the three-dimensional scheme, similar techniques can be applied.

The BGK model in two dimensions case is

$$f_{,t} + uf_{,x} + vf_{,y} = \frac{(g-f)}{\tau}, \tag{2.1}$$

where f is the true gas distribution in space (x, y) and time t, (u, v) are the velocities for a single particle in the $(\hat{x}, \hat{y})$ directions, respectively, and g is the equilibrium state approached by f through collisions. The BGK model can be interpreted as a phenomenological description of the tendency of f under collisions to approach the equilibrium state g on a time scale τ. The relaxation time τ can be a very complicated functional of the distribution f, but for most cases, aside from discontinuity regions, it is reasonable to regard it as a function of the local density and temperature. Owing to the conservation laws of mass, momentum, and energy during particle collisions, the distribution functions of g and f in the BGK model have to satisfy the conservation constraints:

$$\int \begin{pmatrix} 1 \\ u \\ v \\ \frac{1}{2}(u^2+v^2+\xi^2) \end{pmatrix} \frac{(f-g)}{\tau}\, d\Xi = 0, \qquad \forall x, y, t, \tag{2.2}$$

where $d\Xi = \xi^{K-1}\, d\xi\, du\, dv$ corresponds to the differential of the translation velocity and all internal degrees of freedom of the molecules. The connection between the number of internal degrees of freedom K, space dimension D of the simulation and the ratio of specific heats γ of the gas is $K = -D + 2/(\gamma - 1)$. Equation (2.2) determines g completely in terms of f.

On the other hand, in the hydrodynamic limit, the macroscopic description of the gas is specified by the local mass $\rho(x, y, t)$, momentum $\mathbf{P}(x, y, t)$, and energy $\varepsilon(x, y, t)$ densities, which are moments of the true distribution function $f(x, y, t, u, v, \xi)$, defined by

$$\begin{pmatrix} \rho \\ P_x \\ P_y \\ \varepsilon \end{pmatrix} = \int \begin{pmatrix} 1 \\ u \\ v \\ \frac{1}{2}(u^2+v^2+\xi^2) \end{pmatrix} f\, d\Xi. \tag{2.3}$$

The real gas distribution function f has no universal form and can depend on many factors; therefore the local mass ρ, momentum $\mathbf{P}$, and energy ε densities cannot uniquely determine f.

The equilibrium state g should be a stationary state of particle collisions, and the form of g can be derived (Cercignani [8]), namely the Maxwellian

$$g(x, y, t, u, v, \xi) = Ae^{-\lambda((u-U)^2+(v-V)^2+\xi^2)}, \tag{2.4}$$

where the variables A, U, V, and λ are functions of (x, y, t). Given the mass, momentum, and energy densities, there is a uniquely determined equilibrium state g, which can be found by putting g instead of f in the integrals in Eq. (2.3):

$$\begin{pmatrix} \rho \\ P_x \\ P_y \\ \varepsilon \end{pmatrix} = \begin{pmatrix} A\pi^{(K+2)/2}\lambda^{-(K+2)/2} \\ \rho U \\ \rho V \\ \frac{1}{2}\rho\left(U^2+V^2+\dfrac{K+2}{2\lambda}\right) \end{pmatrix}. \tag{2.5a}$$

(We have assumed here that τ does not depend on the variables in $d\Xi$.) For convenience of numerical calculations, we use ρ, λ, U, V instead of A, λ, U, V to describe the Maxwellian distribution. By solving Eq. (2.5a), all parameters in the Maxwellian g can be obtained from the relations

$$\begin{pmatrix} \rho \\ U \\ V \\ \lambda \end{pmatrix} = \begin{pmatrix} \rho \\ P_x/\rho \\ P_y/\rho \\ (K+2)\,\rho/(4(\varepsilon - \frac{1}{2}\rho(U^2+V^2))) \end{pmatrix}. \tag{2.5b}$$

In the following, we give a detailed numerical scheme for calculating the real gas distribution function f at a certain point in two-dimensional space (x, y), then we compute numerical fluxes from f at this point. Consider one point $(x=0, y=0)$ in two-dimensional space as shown in Fig. 1 and assume that at this point, at the beginning of each time step $t=0$, the local equilibrium Maxwellian distribution function is

$$g(x=0, y=0, t=0) = Ae^{-\lambda((u-U)^2+(v-V)^2+\xi^2)}. \tag{2.6}$$

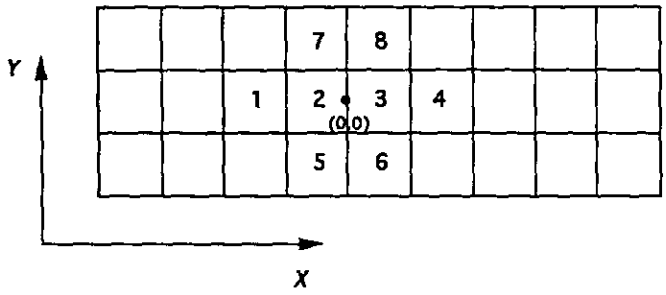

FIG. 1. The two-dimensional domain with the Taylor expansion center at the point (0, 0). The numbers 1 to 8 refer to the cells.

The Taylor expansion of the Maxwellian distribution in the neighborhood of this point (to the first order in space and time) can be written as

$$g(x, y, t) = g(0, 0, 0)(1 + ax + by + \hat{A}t), \tag{2.7}$$

where the coefficients a, b, and $\hat{A}$ have the following dependences on u, v, and ξ:

$$\begin{aligned} a &= a_1 + a_2 u + a_3 v + a_4(u^2 + v^2 + \xi^2), \\ b &= b_1 + b_2 u + b_3 v + b_4(u^2 + v^2 + \xi^2), \\ \hat{A} &= \hat{A}_1 + \hat{A}_2 u + \hat{A}_3 v + \hat{A}_4(u^2 + v^2 + \xi^2). \end{aligned} \tag{2.8}$$

All coefficients $a_1, a_2, ..., \hat{A}_4$ can be regarded as locally constant, and the u, v, ξ dependences arise from the Taylor expansion of the Maxwellian distribution.

Similarly, local initial mass, momentum, and energy densities around the point $(x=0,\ y=0)$ at $t=0$ can be expanded in the forms

$$\begin{aligned} \rho(x, y, 0) &= \rho(0, 0, 0)(1 + \rho_1 x + \rho_2 y) \\ P_x(x, y, 0) &= P_x(0, 0, 0)(1 + P_{x1} x + P_{x2} y) \\ P_y(x, y, 0) &= P_y(0, 0, 0)(1 + P_{y1} x + P_{y2} y) \end{aligned}$$

and

$$\varepsilon(x, y, 0) = \varepsilon(0, 0, 0)(1 + \varepsilon_1 x + \varepsilon_2 y), \tag{2.9}$$

where $\rho(0, 0, 0)$, $\rho_1 \cdots \varepsilon_2$ are also locally defined constants. The interpolation of all macroscopic quantities can be obtained using the so-called TVD or ENO techniques; the difference here is that the interpolated quantities might be across the cell boundary instead of some continuous function inside each cell.

From the mass, momentum, and energy density interpolations at time $t=0$, we can uniquely construct the corresponding equilibrium state $g(0, 0, 0)$, and the a and b terms in Eq. (2.7) by following the relation between macroscopic quantities and the moments of $g(x, y, 0)$. Therefore, the Maxwellian distribution $g(0, 0, 0)$ can be found by using Eq. (2.5b), where ρ, P_x, P_y, and ε are replaced by the interpolated quantities $\rho(0, 0, 0)$, $P_x(0, 0, 0)$, $P_y(0, 0, 0)$, and $\varepsilon(0, 0, 0)$ in Eq. (2.9). After obtaining $g(0, 0, 0)$, the x-dependent a term in Eq. (2.8) can be found as

$$\begin{pmatrix} \rho_1/\rho \\ P_{x1}/\rho \\ P_{y1}/\rho \\ 2\varepsilon_1/\rho \end{pmatrix} = (\mathscr{A}) \begin{pmatrix} a_1 \\ a_2 \\ a_3 \\ a_4 \end{pmatrix}, \tag{2.10a}$$

with

$$(\mathscr{A}) = \begin{pmatrix} 1 & U & V & \mathscr{B}_1 \\ U & U^2 + 1/2\lambda & UV & \mathscr{B}_2 \\ V & UV & V^2 + 1/2\lambda & \mathscr{B}_3 \\ \mathscr{B}_1 & \mathscr{B}_2 & \mathscr{B}_3 & \mathscr{B}_4 \end{pmatrix}, \tag{2.10b}$$

where

$$\begin{aligned} \mathscr{B}_1 &= U^2 + V^2 + (K+2)/2\lambda, \\ \mathscr{B}_2 &= U^3 + V^2 U + (K+4)\, U/2\lambda, \\ \mathscr{B}_3 &= V^3 + U^2 V + (K+4)\, V/2\lambda, \\ \mathscr{B}_4 &= (U^2 + V^2)^2 + (K+4)(U^2 + V^2)/\lambda \\ &\quad + (K^2 + 5K + 8)/4\lambda^2. \end{aligned}$$

Fortunately, the above matrix can be inverted easily, and the solutions for $a_1 \cdots a_4$ can be written in closed form as functions of ρ_1/ρ, ..., $2\varepsilon_1/\rho$. For the b term, we can solve the similar equations using ρ_2/ρ, ..., $2\varepsilon_2/\rho$ on the left-hand side of Eq. (2.10a) and replacing a with b on the right-hand side. At this point, all the unknowns in the linear approximation to the Maxwellian distribution $g(x, y, 0)$ at $t=0$ have been obtained from interpolation of the given initial macroscopic quantities.

The next important question is what the real distribution function $f(x, y, 0)$ is in the neighborhood of the same point $(x=0,\ y=0)$ at $t=0$. In a smooth region we can safely put $f(x, y, 0) = g(x, y, 0)$ under the physical assumption of local thermodynamic equilibrium (LTE). However, if there is a discontinuity near $(x=0,\ y=0)$, f can be a drastically varying function corresponding to different densities, temperatures, and mean velocities, and the assumption $f \approx g$ fails. For numerical purposes, in most cases, the scale size of the numerical grid is much larger than the thickness of the physical discontinuity, and the safest way to proceed here is to interpolate f on both sides of the cell boundary separately. At a shock front, this assumption is consistent with the physical principle that the downstream information cannot propagate upstream past the shock. As shown in the Fig. 1 for the calculation of fluxes in the $\hat{x}$-direction, we can

interpolate all quantities separately in the region $x<0$ and $x>0$, and the resulting distribution function f_0 is taken to be

$$f_0(x, y, 0)=\begin{cases} g^l(0,0,0)(1+a^l x+b^l y), & x<0, \\ g^r(0,0,0)(1+a^r x+b^r y), & x>0, \end{cases} \tag{2.11}$$

where g^l and g^r are both Maxwellians, and a^l, b^l, a^r, and b^r have velocity dependences similar to the a and b terms in Eq. (2.8). In the same way, the mass, momentum, and energy densities can be interpolated as

$$\rho^l(x, y, 0)=\rho^l(0,0,0)(1+\rho_1^l x+\rho_2^l y)$$

$$P_x^l(x, y, 0)=P_x^l(0,0,0)(1+P_{x_1}^l x+P_{x_2}^l y)$$

$$P_y^l(x, y, 0)=P_y^l(0,0,0)(1+P_{y_1}^l x+P_{y_2}^l y)$$

and

$$\varepsilon^l(x, y, 0)=\varepsilon^l(0,0,0)(1+\varepsilon_1^l x+\varepsilon_2^l y), \tag{2.12}$$

for $x<0$, with similar expansions for $\rho^r(x, y, 0)\cdots\varepsilon^r(x, y, 0)$ for $x>0$. In a smooth region the interpolations from the left and right sides are automatically close to each other; near a discontinuity they can have very different values. All parameters in $f_0(x, y)$ can be found in the same way as the quantities appearing in $g(x, y, 0)$ in Eq. (2.7) at time $t=0$.

In paper I we have given an interpolation rule for all conserved quantities in the one-dimensional case. The simplest way to proceed in two dimensions is to use the same interpolation rule to obtain all the x-dependent variables; for example, from the cells (1, 2, 3, 4) in Fig. 1 to interpolate $\rho(0,0,0)$, $P_x(0,0,0)$, ..., ε_1 in Eq. (2.9), as well as the x-dependent terms in Eq. (2.12). There, the main idea of the interpolation is that, by considering four cells (1, 2, 3, 4) centered at $x=0$, we expand the density (and the momentum and energy) in the form $\rho=\rho_0+\rho_1 x+\rho_2 x^2+\rho_3 x^3$, and then we equate the integrated values of these expressions in four different cells to the given average values in these cells, from which the four unknowns ρ_0, ..., ρ_3 can be obtained. After this, we keep just to the linear terms, and drop the x^2 and x^3 terms. If the value of ρ_0 is out of the range of $\rho(2)$ and $\rho(3)$ of the average values in cell (2) and (3), then two cells are used to interpolate ρ_0 and ρ_1. For Eq. (2.12), we use the three cells (1, 2, 3) for the left side interpolation and (2, 3, 4) for the right side ($x=0$ lies on the boundary between cells 2 and 3). Besides this, in this two-dimensional scheme, we need to include the y-dependence as well. The interpolations for the y-dependent variables in Eq. (2.9) and Eq. (2.12) are obtained by using central differences. For example (as shown in Fig. 1),

$$\rho_2=\frac{((\rho(7)+\rho(8))-(\rho(5)+\rho(6)))}{4\rho(0,0,0)},$$

$$\rho_2^l=\frac{((\rho(7)-\rho(5))}{2\rho(0,0,0)}, \tag{2.13}$$

$$\rho_2^r=\frac{(\rho(8)-\rho(6))}{2\rho(0,0,0)}.$$

As recommended by A. Harten and C. Shu, we have tried to use high-order ENO interpolation to obtain these expansion coefficients, but since we keep only linear terms in the current scheme, ENO interpolation does not seem to improve the simulation results appreciably.

Remark. Up to this point, at the beginning of each time step, from the given local mass, momentum, and energy, we have found two distribution functions: one is the equilibrium state $g(x, y, 0)$ in the neighborhood of a cell boundary, and the other is the "real" gas distribution function $f_0(x, y)$ expanded on both sides of the cell boundary.

All expansion coefficients given above refer to $t=0$, and the $\hat{A}$ term of the time-derivative of g in Eq. (2.7) is still unknown. In the following, we use the general solution of the BGK model to determine $\hat{A}$ implicitly from the conservation constraints (cf. Eq. (2.2)). The general integral solution of the BGK model in two dimensions with the above expansions of g and f_0 (for local constant τ) can be written as

$$f(x, y, t)=\frac{1}{\tau}\int_0^t g(0,0,0)(1+ax'+by'+\hat{A}t')\,e^{-(t-t')/\tau}\,dt' + e^{-t/\tau}f_0(x-ut, y-vt), \tag{2.14a}$$

where

$$x'=x-u(t-t'), \qquad y'=y-v(t-t'), \tag{2.14b}$$

are the characteristics of the BGK equation (i.e., the free particle trajectory) for each particle and f_0 is the initial value of the true distribution function at $t=0$.

Using Eq. (2.7), we find, after performing the integration, that

$$\begin{aligned} f(x, y, t)=g(0,0,0)((1-e^{-t/\tau}) & \\ \times(1+ax-\tau ua+by-\tau vb-\tau\hat{A}) & \\ +te^{-t/\tau}(ua+vb)+t\hat{A}) & \\ +e^{-t/\tau}f_0(x-ut, y-vt). & \end{aligned} \tag{2.15}$$

Because we need the fluxes across the boundary at $x=0$ and from $-\frac{1}{2}$ to $\frac{1}{2}$ in the $\hat{y}$-direction, we find that the linear y-dependent term in the above equation disappears when we integrate over dy to obtain fluxes. So, we will need f only at $x=0$, $y=0$. With these simplifications the above equations yields

$$f(0,0,t) = g(0,0,0)((1-e^{-t/\tau}) \times (1-\tau ua - \tau vb - \tau\hat{A}) + te^{-t/\tau}(ua+vb) + t\hat{A}) + e^{-t/\tau}f_0(-ut,-vt), \tag{2.16a}$$

where the initial function f_0 is given by

$$f_0(-ut,-vt) = \begin{cases} g^l(0,0,0)(1-a^l ut - b^l vt), & u>0 \\ g^r(0,0,0)(1-a^r ut - b^r vt), & u<0. \end{cases} \tag{2.16b}$$

The unknown parameter $\hat{A}$ in the above distribution function $f(0,0,t)$ can be obtained by using the time average of the conservation constraints at $(x=0,\ y=0)$ over the duration of the time step T:

$$\int\int_0^T \begin{pmatrix} 1 \\ u \\ v \\ \frac{1}{2}(u^2+v^2+\xi^2) \end{pmatrix} (g(0,0,t)-f(0,0,t))\, d\Xi\, dt = 0. \tag{2.17}$$

From the above equations, we can obtain equations similar to Eq. (2.10a) for $\hat{A}$ by replacing $a_1, ..., a_4$ by the unknown parameters $A_1, ..., A_4$, using the same matrix $\mathscr{A}$ on the right-hand side. The left-hand side will depend explicitly on moments of $g(0,0,0)$, the quantities a, b, and $f_0(-ut,-vt)$. At this point, all parameters in the expression of $f(0,0,t)$ are known (see [33] for more detailed formulas), and we can easily evaluate the final mass, momentum, and energy fluxes across the boundary for the whole time step T. These are

$$\begin{pmatrix} F_\rho \\ F_{P_x} \\ F_{P_y} \\ F_\varepsilon \end{pmatrix} = \int\int_0^T u \begin{pmatrix} 1 \\ u \\ v \\ \frac{1}{2}(u^2+v^2+\xi^2) \end{pmatrix} f(0,0,t)\, d\Xi\, dt. \tag{2.18}$$

The main part of the numerical calculation in this scheme is based on the evaluation of the moments of the Maxwellian. This looks complicated, but owing to the simple recursion relations connecting different moments, the programming is not hard.

The past several years have seen many multidimensional schemes for the Euler equations with improved shock-capturing properties (van Leer [31], Catalano *et al.* [7]); these can be divided into two general classes: one is based on the application of the rotated 1D Riemann solver, and the other is a genuinely multidimensional attack on the equations by separating them into an equivalent set of scalar wave equations with solution-dependent propagation directions. In our scheme, instead of using a set of scalar waves, we have used all particle trajectories. As can be seen from Eq. (2.14b), each particle has a certain characteristic trajectory. The particle can move in any direction in the two-dimensional space with velocity (u, v), and these directions are not restricted to the mesh directions. This property separates this scheme from simple directional splitting codes, and this difference is clearly demonstrated in the shock reflection test case in the following section.

III. NUMERICAL NAVIER–STOKES AND EULER SOLUTIONS

From gas-kinetic theory, the physical collision time is given by $\tau = l/\bar{v}$, where l is the mean free path, which can be written as a function of local number density n and the molecular cross section σ as $l \propto 1/n\sigma$, and the mean gas velocity $\bar{v}$ is proportional to the square-root of the gas temperature. Hence, the collision time can be written as

$$\tau = \mathscr{C}_1 \frac{\sqrt{\lambda}}{\rho(0,0,0)}, \tag{3.1}$$

where both the temperature parameter λ ($\lambda = 1/k\bar{T}$, where k is the Boltzmann constant and $\bar{T}$ is the temperature) and the density $\rho(0,0,0)$ are chosen to correspond to the interpolated quantities for $g(0,0,0)$. All proportionality constants are included in the parameter $\mathscr{C}_1$.

From kinetic theory, the relation between the collision time and dynamical viscosity is

$$\eta = \tau p, \tag{3.2}$$

where p is gas pressure. The kinematic viscosity ν is defined as $\nu = \eta/\rho$. The dimensionless Reynolds number Re is given by $\mathrm{Re} = UL/\nu$, where U and L are characteristic velocity and length scales. For numerical purposes, we can find the parameter $\mathscr{C}_1$ in terms of other known quantities,

$$\mathscr{C}_1 = \left(\frac{UL}{\mathrm{Re}}\right)\left(\frac{\rho^2(0,0,0)}{\sqrt{\lambda}\, p}\right), \tag{3.3}$$

where the velocity U can also be expressed as a function of the Mach number $\mathscr{M}$ and the sound speed c.

In order to validate the applicability of this gas kinetic scheme as a Navier–Stokes solver, in the following we give

two well-defined Navier–Stokes test cases using $\gamma = 1.4$ in both cases:

(1) The Kolmogorov test case is taken from a paper about a lattice gas method by P. Kornreich and J. Scalo [18]. We use this one-dimensional shear flow example to illustrate the viscosity effects in our numerical scheme. Initially the $\hat{x}$-component of velocity is $u_x = u_0 \sin(2\pi y/\mathscr{L})$ with $u_0 = 0.5$ and the $\hat{y}$-component is $u_y = 0$. Our simulation uses a 64×64 grid with initial homogeneous mass density $\rho = 1.0$ and thermal energy density $\varepsilon_t = 0.67$, where the wavelength $\mathscr{L}$ is 64 and the periodic boundary conditions are assumed in both directions. Since no perturbations are included in the initial data, the velocity profile keeps the same shape with decreasing $\hat{x}$-velocity amplitude as the solution evolved. In order to study viscosity effects quantitatively we have compared the kinetic energy decay rate obtained from the solution of the exact Navier–Stokes equations with the results from our numerical simulation. Since the initial kinetic energy density $\varepsilon_k = 0.125$ is much less than the thermal energy $\varepsilon_t = 0.67$, we can regard pressure, density, and temperature as nearly constant and ignore the variation of the dynamic viscosity η in space and time. By solving the Navier–Stokes equations, we obtain

$$\frac{E(t)}{E(0)} = \exp\left[-\mathscr{C}_1 \left(\frac{2\pi}{\mathscr{L}}\right)^2 \sqrt{2p/\rho^3}\, t \right], \tag{3.4}$$

where t is the time. Using $E(t)/E(0) = e^{-\nu_{NS} t}$ to replace the above equation, we find the viscosity coefficient for the exact solution to be

$$\nu_{NS} = \mathscr{C}_1 \left(\frac{2\pi}{\mathscr{L}}\right)^2 \sqrt{2p/\rho^3}. \tag{3.5}$$

We have run this case by using our code up to time $t = 1000$ for six different values of the parameter $\mathscr{C}_1$. By fitting our numerical results at $t = 1000$ to $E(t)/E(0) = e^{-\nu_{exp} t}$, we can obtain the corresponding experimental coefficient ν_{exp}. Table I shows the comparison between the theoretical values and the experimental ones for different $\mathscr{C}_1$. From Table I it is clear that this code gives a numerical

TABLE I

Quantitative Viscous Effects

C_1 coefficients	ν_{NS}	ν_{exp}
0.01	7.0563×10^{-5}	6.984×10^{-5}
0.03	2.1169×10^{-4}	1.982×10^{-4}
0.05	3.528×10^{-4}	3.134×10^{-4}
0.07	4.939×10^{-4}	4.162×10^{-4}
0.10	7.0563×10^{-4}	5.781×10^{-4}
0.20	1.411×10^{-3}	8.501×10^{-4}

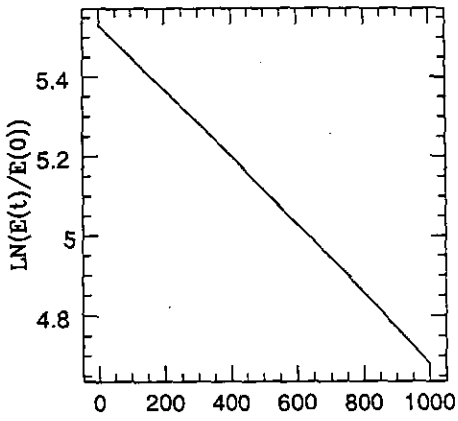

FIG. 2. Kolmogorov test case; $\ln(E(t)/E(0))$ is plotted as a function of time.

Navier–Stokes solution in this case and the difference between the numerical and exact solutions becomes smaller for smaller collision time τ. The difference between them becomes obvious with increasing $\mathscr{C}_1$. The reason for this difference is that, in this problem, the CFL time step is about $T \sim 0.60$, and the collision time is $\tau = 1.366\mathscr{C}_1$. As $\mathscr{C}_1$ increases, the collision time becomes closer to the time step, and we approach the situation where the problem should be treated by rarefied gas dynamics. Actually, this is beyond the present scope of our code. In order to confirm the exponential kinetic energy decay effect, we also give a plot of $\ln(E(t)/E(0))$ as a function of time in Fig. 2; the slope of the line gives the exponential decay rate.

(2) The laminar boundary layer problem with a leading edge is taken from a paper by Allmaras [2]. The flowfield evolves above a flat plate (located along the $\hat{x}$-direction) at zero incidence. The free stream Mach number is $M_\infty = 0.3$

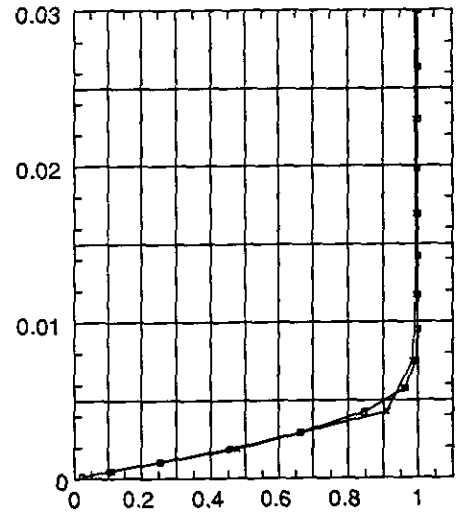

FIG. 3. Boundary layer simulation with eight cells (×) and 16 cells (□) in the direction perpendicular to the flat plate.

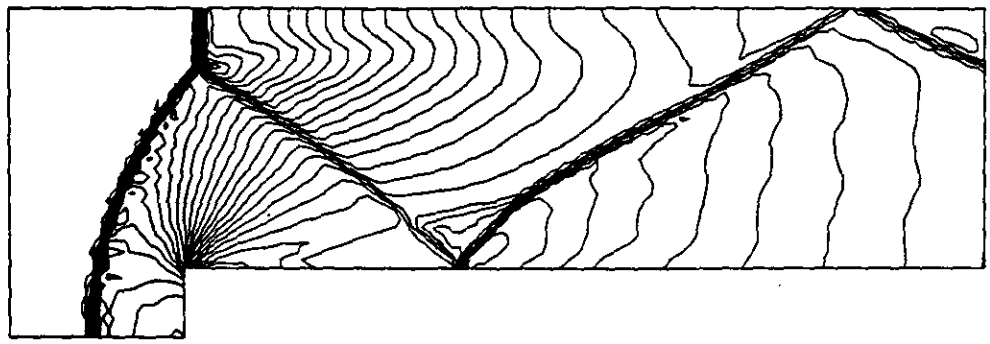

FIG. 4. Mach 3 flow in a wind tunnel with a step; 30 density contours are plotted on a 120×40 grid.

and the Reynolds number is $\mathrm{Re} = 500{,}000$ per unit length. From the value of M_∞ and for initial mass and momentum densities $\rho = 1.0$, $P_x = 1.0$, $P_y = 0.0$, we can find the initial internal energy. Together with the kinetic energy, the total energy density is $\varepsilon_t = 20.34126984$. At the same time, from the Reynolds number Re and Eq. (3.3), we find the parameter $\mathscr{C}_1$, which is $\mathscr{C}_1 = 1.0030 \times 10^{-6}$. The computational domain is a rectangle extending 0.54 units upstream of the leading edge and 1.50 units downstream. The upper boundary is located 0.03 units above the flat plate. The grids are parabolically stretched away from the leading edge in the $\hat{x}$-direction, symmetrically upstream and downstream of the leading edge. The grids are also stretched parabolically away from the lower boundary in the upward $\hat{y}$-direction. Two computational domains of 32×16 and 16×8 are used in this boundary layer problem. No-slip boundary conditions are imposed on the flat plate, compatible with the Navier–Stokes equation. On the top and left boundaries all quantities retain the initial input flow conditions, and on the right boundary the free flow condition is applied. In this simulation, because of the non-uniformity of the grid sizes, we have used simpler initial interpolations for the mass, momentum, and energy at the beginning of each time step. For all quantities, we assign the cell average values to the volume center and use linear interpolation along the line connecting the volume centers. The time step is determined by the CFL condition and the output time in Fig. 3 is the time needed for the gas moving at the free stream velocity to get from the left end of the flat plate to the right end. The output at the mid-point of the plate for the $\hat{x}$ directional velocity distribution on the line perpendicular to the flat plate is shown in Fig. 3, where the curve from 32×16 meshes is almost identical to the converged Navier–Stokes solutions in Allmaras's paper.

From above test cases, we see that the true real viscosity effects are captured by our numerical scheme. In the laminar boundary layer problem, since the grid size is smaller than the boundary layer structure, there is no need to add additional artificial viscosity to stabilize our scheme. To test this assertion, we increased the cell size next to the flat plate to a value larger than the boundary layer thickness, and we find that oscillations emerge near the boundary. In order to reduce these oscillations, a larger collision time is needed, which is equivalent to adding additional viscosity (cf. Eq. (3.2)) to widen the numerical boundary layer thickness to a scale larger than one or two grid sizes. Physically, this is the same mechanism as suppressing the postshock oscillations by increasing the dissipation.

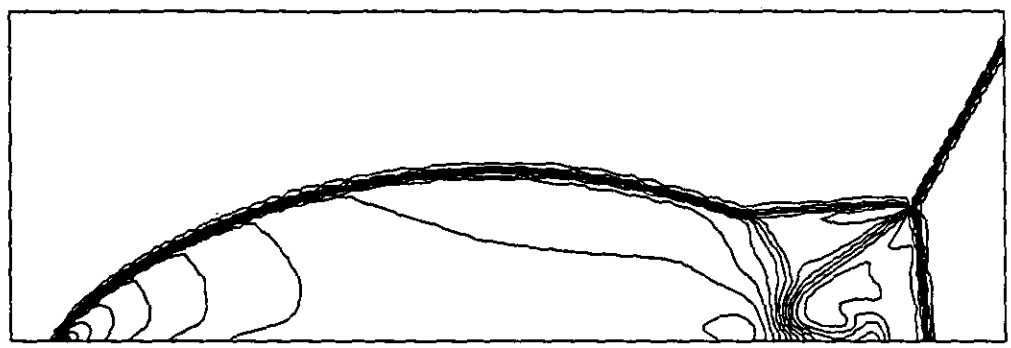

FIG. 5. Double Mach reflection test case with 30 density contours on the domain 180×60.

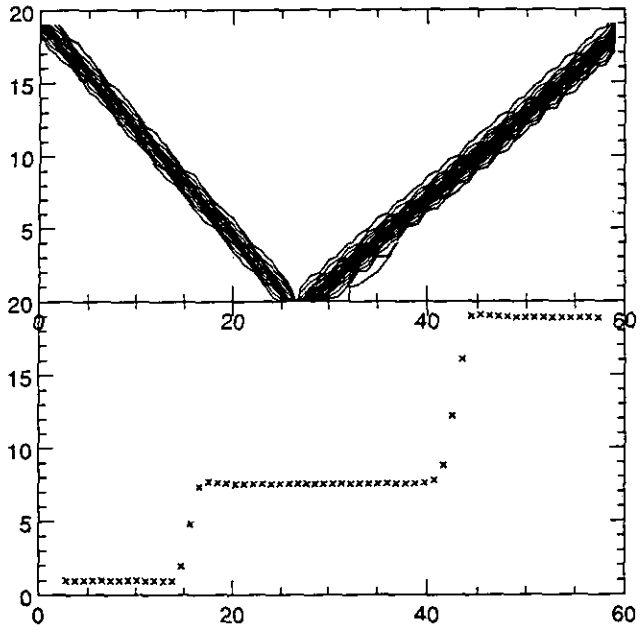

FIG. 6. Steady state solution of the regular shock reflection. Thirty equally distributed density contours are shown in (a), and the pressure profile along the line $y = 0.525$ is plotted in (b).

We can use the same expression for the collision time in the case of strong shocks,

$$\tau = \mathscr{C}_1 \frac{\sqrt{\lambda}}{\rho(0,0,0)} + \mathscr{C}_2 \sqrt{\lambda} \times \frac{|\sqrt{\lambda^l}/\rho^l(0,0,0) - \sqrt{\lambda^r}/\rho^r(0,0,0)|}{\sqrt{\lambda_0^l}/\rho^l(0,0,0) + \sqrt{\lambda_0^r}/\rho^r(0,0,0)} \times \frac{|p^l - p^r|}{p^l + p^r}, \tag{3.6}$$

where the pressures p^l and p^r and the temperatures λ^l and λ^r terms are obtained from $g^l(0,0,0)$ and $g^r(0,0,0)$. The second term in the above equation can be understood from the requirement that the discontinuity thickness should be comparable with the grid size. Another explanation for the second term can be this: in the discontinuity region, owing to the steep slopes for the mass, momentum, and energy interpolations, negative density or temperatures can easily occur in the region close to the cell boundary, which would create pseudo-particles to deteriorate the numerical fluxes in our scheme. The second term just reduces these effects exponentially. In a smooth region, the second term is always small.

We know that the Navier–Stokes equations approach the Euler equations when the real viscosity becomes very small. In the following we gave the results of three well-defined Euler test cases, where $\mathscr{C}_1 = 0.01$ and $\mathscr{C}_2 = 1.0$ are used in Eq. (3.6) in all instances.

(3) The third test is the same Emery test as discussed in paper I with a computational domain 120×40. Figure 4 shows the result from our current 2D code: the second Mach stem is shorter than the one from the splitting scheme in paper I. No special treatment of the cells near the step corner was employed in this calculation.

(4) The fourth test is the case of double Mach reflection of a strong shock, taken from a paper by Woodward and Colalla [32]. The computational domain is 240×60, but here we plot 30 contours in the region of 180×60. As can be seen in Fig. 5, we obtain very sharp shock fronts.

(5) The last test case is regular shock reflection. The computational domain is a rectangle of length 4 and height 1 divided into a 60×20 rectangular grids with $\Delta x = \frac{1}{15}$, $\Delta y = \frac{1}{20}$. Dirichlet conditions

$$(\rho, u, v, p)|_{(0,y,t)} = (1.0, 2.9, 0.0, 1/1.4),$$

$$(\rho, u, v, p)|_{(x,1,t)} = (1.69997, 2.61934, -0.50633, 1.52819).$$

are imposed on the left and upper boundaries, respectively. The bottom boundary is a reflecting wall and the supersonic outflow condition is applied along the right boundary. Initially, the solution in the entire domain is set to be that at the left boundary [11]. We iterate for 500 time steps, at which time the solution reaches a steady state. Figure 6 shows the result from this 2D code.

IV. CONCLUSION

In this paper we have extended the gas kinetic based hydrodynamic scheme in paper I to two dimensions. This scheme solves the hydrodynamic equations numerically by following the integral solution of the BGK model. As pointed out in paper I, there are some advantages to the gas kinetic approach to numerical hydrodynamics. In [33], more detailed analysis of our schemes are given.

Linear interpolations for all conserved quantities are used in all test cases, and the simulation results have high resolution. The reason is that the time evolution of the distribution functions are followed explicitly from the initial linear interpolation. Here second-order resolution in both space and time are achieved without using intermediate stages. Also, the implicit way we obtained the term $\hat{A}$ in Eq. (2.7) allows this Navier–Stokes scheme to use a CFL timestep $\delta t = \mathscr{O}(\Delta x)$.

We include both $\partial/\partial x$ and $\partial/\partial y$ at the same time, which is an advance on the directional splitting scheme (paper I), where just one of them is included. Even in the direction splitting version of our scheme, which deletes $\partial/\partial y$ when calculating $\hat{x}$ directional fluxes, the $\hat{y}$-momentum transfer can still be counted and solved explicitly in the $\hat{x}$-direction. This is different from most Godunov schemes, where one-

dimensional Riemann solvers are used for two-dimensional simulations. Sometimes, the inclusion of $\hat{y}$-momentum is crucial for one-dimensional shear flows, such as for the calculation of the Rayleigh problem (Chu [10]) of viscous flow adjacent to an impulsively started moving wall.

Since all trajectories (characteristics) of individual particles are followed, it is possible to make this scheme more multidimensional by careful interpolation of the initial quantities. This property is different from other multidimensional schemes starting from the Euler or Navier–Stokes equations directly, where local decompositions into a finite number of traveling waves are used (Rumsey *et al.* [26]).

It would not be hard to include second- and third-order Taylor expansions for g and f, carrying $\partial^2/\partial x\,\partial y$, $\partial^2/\partial x\,\partial t$, etc. and evaluating their coefficients explicitly, using derivatives of the conservation constraints. However, this would make the code not only more sensitive to the precise form of the initial interpolation, but it would also greatly increase the computational time. For turbulence flow simulations, including high-order terms may be worthwhile.

ACKNOWLEDGMENTS

We thank Ami Harten, Chi-Wang Shu, and Peter Lax for helpful discussions, and Philip Roe for carefully reviewing the first draft of this paper and suggesting additional numerical test cases. K.X. also thanks J. H. van Gorkom for financial support during the past summers in Columbia.

REFERENCES

1. M. Abramowitz and I. Stegun, *Handbook of Mathematical Functions*, Dover, New York, 1972.
2. S. R. Allmaras, "Contamination of Laminar Boundary Layers by Artificial Dissipation in Navier-Stokes Solutions," in *Fourth Conference on Numerical Methods for Fluid Dynamics, Reading University, UK, April 1992.*
3. P. L. Bhatnagar, E. P. Gross, and M. Krook, *Phys. Rev.* **94**, 511 (1954).
4. G. A. Bird, *Molecular Gas Dynamics* (Clarendon Press, Oxford, 1976).
5. J. P. Boon, "Statistical Mechanics and Hydrodynamics of Lattice Gas Automata," in *Lattice Gas Methods*, edited by Gary D. Doolen (Addison–Wesley, Reading, MA, 1991).
6. J. E. Broadwell, *Phys. Fluids* **7**, 1243 (1964).
7. L. A. Catalano, P. DePalma, and P. Pascazio, in *Proceedings, 13th International Conference on Numerical Methods in Fluid Dynamics*, Lecture Notes in Physics, Vol. 414 (Springer-Verlag, New York/Berlin, 1992).
8. C. Cercignani, *The Boltzmann Equation and Its Applications*, Springer-Verlag, New York/Berlin, 1988).
9. C. K. Chu, *Phys. Fluids* **8**, 12 (1965).
10. C. K. Chu, "The High Mach Number Rayleigh Problem According to the Krook Model," in *Rarefied Gas Dynamics, 5th Symposium*, Vol. 1, 1967.
11. P. Colella, *J. Comput. Phys.* **87**, 171 (1990).
12. G. D. Doolen (Ed.), *Lattice Gas Methods for Partial Differential Equations* (Addison–Wesley, Reading, MA, 1990).
13. U. Frisch, D. d'Humieres, B. Hasslacher, P. Lallemand, Y. Pomeau, and J. P. Rivet, *Complex Systems* **1**, 632 (1987).
14. A. Harten, "Preliminary Results on the Extension of ENO Schemes to Two-Dimensional Problems," in *Proceedings, International Conference on Hyperbolic Problems, Saint-Etienne, January 1986.*
15. A. Harten, P. D. Lax, and B. van Leer, *SIAM Rev.* **25** (1983).
16. A. Jameson, W. Schmidt, and E. Turkel, AIAA Paper 81-1259, 1981 (unpublished).
17. B. Koren, "Upwind Schemes for the Navier–Stokes Equations," in *Notes on Numerical Fluid Mechanics*, Vol. 24, edited by J. Ballmann and R. Jeltsch (Vieweg, Brunswick, 1989).
18. P. Kornreich and J. Scalo, preprint, Department of Astronomy, University of Texas as Austin; *Physica D*, submitted.
19. R. W. MacCormack, AIAA Paper 69-354, 1969 (unpublished).
20. L. Martinelli and A. Jameson, AIAA Paper 88-0414, 1988 (unpublished).
21. B. Perthame, *SIAM J. Numer. Anal.* **29**, No. 1 (1992).
22. K. H. Prendergast and K. Xu, *J. Comput. Phys.* **109**, 53 (1993).
23. D. I. Pullin, *J. Comput. Phys.* **34**, 231 (1980).
24. Y. H. Qian, D. d'Humieres, and P. Lallemand, *Europhys. Lett.* **17**(6), 479 (1992).
25. P. L. Roe, *J. Comput. Phys.* **63**, 458 (1986).
26. C. L. Rumsey, B. van Leer, and P. L. Roe, *J. Comput. Phys.* **105**, 306 (1993).
27. R. H. Sanders and K. H. Prendergast, *Astrophys. J.* **188** (1974).
28. H. Schlichting, *Boundary Layer Theory*, McGraw–Hill, New York, 1979.
29. C. W. Shu, T. A. Zang, G. Erlebacher, D. Whitaker, and S. Osher, *Appl. Numer. Math.* **9**, 45 (1992).
30. B. van Leer, in *Computing Methods in Applied Sciences and Engineering VI*, edited by R. Glowinski and J. L. Lions (North-Holland, Amsterdam, 1984), p. 493.
31. B. van Leer, "Progress in Multidimensional Upwind Differencing," in *Proceedings, 13th International Conference on Numerical Methods in Fluid Dynamics*, Lecture Notes in Physics, Vol. 414 (Springer-Verlag, New York/Berlin, 1992).
32. P. Woodward and P. Colella, *J. Comput. Phys.* **54**, 115 (1984).
33. K. Xu, Ph.D. thesis, Columbia University, September 1993.